DOT/FAA/AR-11/1,P2

Federal Aviation Administration
William J. Hughes Technical Center
Aviation Research Division
Atlantic City International Airport
New Jersey 08405

Adhesively Bonded Joints

Part 2: The Cohesive Zone Model for Analysis of Fracture and Damage Tolerance of Adhesively Bonded Joints

February 2014

Final Report

This document is available to the U.S. public through the National Technical Information Services (NTIS), Springfield, Virginia 22161.

This document is also available from the Federal Aviation Administration William J. Hughes Technical Center at actlibrary.tc.faa.gov.

U.S. Department of Transportation
Federal Aviation Administration

NOTICE

This document is disseminated under the sponsorship of the U.S. Department of Transportation in the interest of information exchange. The U.S. Government assumes no liability for the contents or use thereof. The U.S. Government does not endorse products or manufacturers. Trade or manufacturers' names appear herein solely because they are considered essential to the objective of this report. The findings and conclusions in this report are those of the author(s) and do not necessarily represent the views of the funding agency. This document does not constitute FAA policy. Consult the FAA sponsoring organization listed on the Technical Documentation page as to its use.

This report is available at the Federal Aviation Administration William J. Hughes Technical Center's Full-Text Technical Reports page: actlibrary.tc.faa.gov in Adobe Acrobat portable document format (PDF).

Technical Report Documentation Page

1. Report No.	2. Government Accession No.	3. Recipient's Catalog No.
DOT/FAA/AR-11/1,P2		

4. Title and Subtitle	5. Report Date
ADHESIVELY BONDED JOINTS, PART 2: THE COHESIVE ZONE MODEL FOR ANALYSIS OF FRACTURE AND DAMAGE TOLERANCE OF ADHESIVELY BONDED JOINTS	February 2014
	6. Performing Organization Code
7. Author(s) Thomas Siegmund	8. Performing Organization Report No.
9. Performing Organization Name and Address Purdue University 155 S. Grant Street West Lafayette, IN 47907-2114	10. Work Unit No. (TRAIS)
	11. Contract or Grant No.
12. Sponsoring Agency Name and Address U.S. Department of Transportation Federal Aviation Administration Aviation Safety—Aircraft Certification Service—Aircraft Engineering Division 1601 Lind Ave., SW Renton, WA 98057	13. Type of Report and Period Covered Final Report 2004-2010
	14. Sponsoring Agency Code AIR-100

15. Supplementary Notes

The Federal Aviation Administration William J. Hughes Technical Center Aviation Research Division Technical Monitor was Lynn Pham.

16. Abstract

This report details work conducted at Purdue University under the Federal Aviation Administration (FAA) Joint Advanced Materials and Structures Center of Excellence program on adhesively bonded structures, and it addresses the issues of the correlation between bondline thickness and fracture, as well as the design of hybrid adhesively bonded joints. This report is one of three reports that were generated by the FAA program.

As an alternative to the fracture mechanics concepts and the critical crack tip angle approach to joint characterization, cohesive zone modeling has emerged as a capable tool for simulation of fracture processes. The cohesive zone model (CZM) can overcome the limitations and disadvantages of conventional fracture mechanics. However, material data for the CZM is lacking. To overcome this obstacle, this research attempts to show how such material data could effectively be measured. The structural adhesive Hysol® EA 9394™ was used to demonstrate this approach. A study on the transferability of measured cohesive model parameters for this adhesive was conducted using a similar but larger double cantilever beam. Subsequently, mode I cohesive zone parameters were used to predict the mode mixity dependence of the initiation toughness for this adhesive. Thereby, a CZM was embedded into the extended finite element method framework.

17. Key Words	18. Distribution Statement
Fracture mechanics, Local failure criterion, Cohesive zone model, Adhesive bonding	This document is available to the U.S. public through the National Technical Information Service (NTIS), Springfield, Virginia 22161. This document is also available from the Federal Aviation Administration William J. Hughes Technical Center at actlibrary.tc.faa.gov.

19. Security Classif. (of this report)	20. Security Classif. (of this page)	21. No. of Pages	22. Price
Unclassified	Unclassified	35	

Form DOT F 1700.7 (8-72) Reproduction of completed page authorized

TABLE OF CONTENTS

			Page
EXECUTIVE SUMMARY			vii
1.	INTRODUCTION		1
2.	MODE I LOADING OF ADHESIVELY BONDED JOINTS		2
	2.1	Experiments on DCB Specimens	2
		2.1.1 Materials	2
		2.1.2 Specimens	3
		2.1.3 Test Procedures	4
		2.1.4 Analysis Methodology	6
		2.1.5 Model Implementation	6
	2.2	Results on DCB Specimens Under Quasistatic Loading	7
		2.2.1 Load Displacement Records	7
		2.2.2 Validity of a Nonlinear-Elastic Analysis Approach to Joint Failure	9
		2.2.3 Determination of Cohesive Zone Law	11
		2.2.4 Simulation Results	13
		2.2.5 Strain Fields Near the Crack Tip and Crack Opening	14
		2.2.6 Transferability of Crack Growth Characterization	17
		2.2.7 Measurement and Prediction of the CTOA	18
3.	MIXED-MODE LOADING		19
	3.1	Analysis Approach	19
		3.1.1 The Extended Finite Element Method	19
		3.1.2 Model Definition	20
	3.2	Results on Mixed-Mode Toughness	20
4.	CONCLUSIONS		23
5.	REFERENCES		24

LIST OF FIGURES

Figure		Page
1	Specimen Group 1: Specimen Geometry and Actual Specimen	3
2	Experiment Setup	5
3	Model Geometry and Representative 3D Finite Element Mesh for Specimen Group 1	7
4	Experimental Results of Specimen Group 1	8
5	Fracture Surfaces of Specimen Group 1	9
6	Surface Images and Fracture Reconstruction	11
7	Determination of Cohesive Traction-Separation Law for the Adhesive	12
8	Comparison of Finite Element Simulation Results and Experimental Data for Specimen Group 1: Force Deflection Response and Crack Extension	13
9	Strain Field Comparison: Strain Field From Experiments, Strain Field Computization of the 2D Model, Strain Field Computation of Side Surface From the 3D Model, and Strain Field Computation of Mid-Plane From the 3D Model	15
10	Predicted Crack Tip-Opening Displacements in the Plane-Strain and 3D Simulations	16
11	Comparison of Finite Element Simulation Results and Experimental Data Force Deflection Response, Specimen Group 2	18
12	Experimental Data on CTOA and Finite Element Predictions	19
13	The Crack Tip Region of the Joint Submodel	20
14	Predicted Mixed-Mode Toughness of Adhesively Bonded Joints	22
15	Crack Tip and Crack Path in an Adhesively Bonded Joint Loaded Under Mode II Conditions	22
16	Simulated Crack Paths Under Mode II Loading: Thin Bondline and Thick Bondline	23

LIST OF TABLES

Table		Page
1	The Material Properties of Adhesive and Aluminum Adherend	3

LIST OF ACRONYMS

2D	Two-dimensional
3D	Three-dimensional
CTOA	Crack tip-opening angle
CZM	Cohesive zone model
DCB	Double cantilever beam
DIC	Digital image correlation
ENF	End notch flexure
FAA	Federal Aviation Administration
MMB	Mixed-mode bend
N	Newton
XFEM	Extended finite element method

EXECUTIVE SUMMARY

This report details work conducted at Purdue University under the Federal Aviation Administration (FAA) Joint Advanced Materials and Structures Center of Excellence program, which advances knowledge on adhesively bonded structures and addresses the issues of the correlation between bondline thickness and fracture, as well as the design of hybrid adhesively bonded joints. This report is one of three reports that were generated by the FAA program.

As an alternative to the fracture mechanics concepts and the critical crack tip angle approach to joint characterization, cohesive zone modeling has emerged as a capable tool for simulating fracture processes. The basic concept of the cohesive zone model (CZM) is to account for the material separation by introducing a softening traction-separation law at the process zone, thereby removing the stress singularity by using the softening traction-separation law at the process zone. Furthermore, the initial idea of a single crack growth into a known direction under pure mechanical loading was extended. The CZM can overcome the limitations and disadvantages of conventional fracture mechanics. However, material data for the CZM are lacking. To overcome this obstacle, this research attempts to show how such material data could effectively be measured. The structural adhesive Hysol® EA 9394™ was used to demonstrate this approach. A study on the transferability of measured cohesive zone parameters for this adhesive was conducted. Subsequently, mode I cohesive zone parameters were used to predict the mode mixity dependence of the initiation toughness for this adhesive, thereby embedding a CZM into the extended finite element method framework.

Furthermore, special attention was paid to the transferability (i.e., application to joint configurations other than that from which cohesive zone law was measured) and geometry independence of the CZM approach in this study. The cohesive zone law obtained from experiments was very successful at simulating the experimental results conducted in geometry configuration other than that from which the cohesive zone law was measured. The simulation results of both global force load-line displacement and local crack tip-opening angle (CTOA) behavior were in good agreement with the experiment data. This validates that the cohesive zone is geometry-independent and can be used as the material parameter to apply in different geometry configurations. From the simulations, it was also shown that the CTOA constant value in the steady-state is size-independent for the double cantilever beam samples considered in this study. CTOA value predicted from a three-dimensional model was slightly higher than the value predicted from a two-dimensional model.

A CZM was developed that allows for the prediction of mixed-mode crack growth resistance of adhesively bonded joints of varying joint thickness. It was demonstrated that crack path selection can be a major contribution to joint toughness if the mode mixity is high and the bondline thickness is large. In this case, the crack path develops freely. However, if the bondline thickness is small, the constraint imposed does not allow the crack path to develop, and the crack is forced, rather, into a mode I situation. The toughness, then, is that of a mode I loaded joint. The increased toughness of the kinked crack paths enables the selection of different fracture modes, if a particular adhesive possesses such features. Then, a high crack path deflection will compete with alternative, lower toughness crack paths and a bimodal toughness response can be

expected. The model presented is based on a basic energy criterion of crack advance and can be readily expanded to mode complex joint configurations. Experimental validation of the model is still necessary, despite that fact that the trends predicted by the model are in good agreement with general findings in related studies.

1. INTRODUCTION.

Significant amounts of both primary and secondary load-bearing structures in aerospace equipment and vehicles are constructed by joining members through the use of structural adhesives. Composite-to-metal tubular lap joints are also widely used in applications ranging from joining composite drive shafts to metal end fittings in automobiles, and joining composite blades to metal hubs in wind turbines [1 and 2]. The use of adhesively bonded joints in critical structural applications necessitates the development of integrity assessment methodologies. It is well-known that failure prediction remains a difficult problem in composites and in adhesively bonded joints. For adhesively bonded, built-up structures, failure is even more difficult to predict due to the complexity of geometric details and loading variability. Analysis of such joints requires the knowledge of the fracture and the failure behavior of the adhesive. The ability to predict failure is a necessary technology for reasons related to safety, performance, and cost. Delaminations within a joint are often difficult to detect and yet can potentially lead to catastrophic failure. The objective of this study was to investigate crack growth in a widely used structural adhesive. The adhesive selected for the study was Hysol® EA9394™.

The cohesive zone model (CZM) approach was initially proposed in reference 3 as an alternative concept to fracture mechanics and later extended in references 4 through 6 to modern applications. The basic concept of the CZM is to account for material separation by introducing a softening traction-separation law at the process zone, thereby removing the stress singularity by using the softening traction-separation law at the process zone. Furthermore, the initial idea of a single crack growth into a known direction under pure mechanical loading was extended. Recent advances in computational mechanics have established the CZM approach in the context of the extended finite element method (XFEM) such that arbitrary directions of crack growth can be considered [7 and 8] and in cases where mechanical loading and chemical changes are accounted for [9]. While the basic CZM is relevant for material characterization in the laboratory, arbitrary loading directions are a concern for bonded joints in composite structures.

The CZM approach was introduced in the study of adhesively bonded joints in several past studies [10-14]. In reference 12, the authors used the CZM on the interface to investigate the influence on joint toughness of both the elastic mismatch between the layer and the substrates and the residual stress in the layer. Later, in references 13 and 14, the CZM was applied to simulate the fracture process of adhesively bonded beams undergoing extensive plastic deformation of the adherends for mode I, mode II, and mixed-mode loading conditions. Nevertheless, the need to study how to extract the cohesive zone law from the adhesive itself remains. The existing CZM, as applied in adhesively bonded joints, was mostly obtained by calibrating the parameter of the assumed cohesive law shape through the comparison of the global specimen behavior between the simulation and the experimental measurements, e.g., reference 15. This approach can lead to good results for the global behavior, such as force displacement, instead of the local behavior, such as strain field around the crack tip. However, a detailed understanding of the fracture process is needed by measuring not only the global specimen behavior, but also the local behavior in the vicinity of crack tip [16].

Adhesively bonded joints are commonly subjected to loading configurations that are not pure mode I. Extensive laboratory studies have been conducted to obtain the dependence of the toughness of adhesively bonded joints with contribution of the mode II loading. Typically, specimen geometries such as the double cantilever beam (DCB) (for mode I), the mixed-mode bend (MMB) (for mixed loading conditions), and the end notch flexure (ENF) (for mode II) configurations are used, as documented in this report. Based on such experiments, a dependence of the total energy release rate on the mode mixity angle is established. Mode mixity is thereby expressed as the ratio between the mode II energy release rate component to the mode I energy release rate component. For most adhesives, the joint toughness increases with the increase in mode mixity. Nevertheless, situations exist where the findings are more complex and where the increase in mode mixity either does not increase the total toughness or leads to a decrease in toughness. Such considerations regarding the mixed-mode fracture toughness of adhesively bonded joints disregards the events locally at the crack tip during crack initiation and propagation. It has been demonstrated that crack path selection plays a significant role in the failure processes of adhesively bonded joints. It is mostly unknown how the crack path selection depends on the adhesively bonded joint thickness, the material parameters characterizing the adhesive, and the material separation processes. This report documents an approach to the determination of the mixed-mode toughness of adhesively bonded joints under consideration of bondline thickness effects. The basis for the analysis approach is the use of a CZM within the extended finite element method, thereby solving the crack path selection problem within the adhesively bonded joint in a general form, and the mixed-mode fracture toughness can be predicted based on mode I fracture experiments only.

In section 2, the CZM is developed using tests on the geometry of one DCB specimen, and the CZM is then applied to a larger DCB specimen and compared to the tests. In section 3, the CZM is extended to mixed-mode fracture (modes I and II).

2. MODE I LOADING OF ADHESIVELY BONDED JOINTS.

2.1 EXPERIMENTS ON DCB SPECIMENS.

2.1.1 Materials.

The adhesive Hysol EA-9394 (Loctite® Corporation) is a two-part structural epoxy paste adhesive. It can be cured at room temperature for 3 to 5 days or at high temperature (up to 200°F/93°C) to accelerate cure. This adhesive combines high-temperature performance with good strength and toughness. Its thixotropic nature and excellent high-temperature compressive strength also make it ideal for potting, filling, and liquid shim applications. The relevant material properties of the Hysol EA-9394 adhesive [1 and 2] and the aluminum adherends are listed in table 1.

Table 1. Material Properties of Adhesive and Aluminum Adherend [1 and 2]

Material	Elastic Modulus (MPa)	Poisson's Ratio	Yield Strength (MPa)	Hardening Modulus (MPa)
Adhesive	$E_h = 4242.0$	$\nu_h = 0.37$	$\sigma_{y,h} = 30.0$	$E_{h1} = 2040.0$
Aluminum Adherend	$E_{Al} = 70.0\times10^3$	$\nu_{Al} = 0.33$	–	–

For mechanical loading studies, DCB specimens were made by bonding two aluminum adherends with Hysol EA-9394 adhesive. The aluminum surfaces were prepared for bonding by rubbing with 220-grit sandpaper. Then, ethyl alcohol was used to remove residue remaining on the surface. A silane solution (3-Glycidyloxypropyl-trimethoxysilane, 98%, Sigma-Aldrich®) was applied on the aluminum surface to improve bonding. The bondline thickness of the adhesive was controlled by inserting a spacer with specified thickness at the ends of the specimen. After evenly spreading the adhesive on each of the two aluminum adherends, a weight is placed on top of the specimen to achieve the desired bondline thickness by squeezing excess adhesive out. Subsequently, the adhesive was cured for 1 hour at 150°F.

2.1.2 Specimens.

Two different DCB specimens were fabricated. For group 1, the DCB specimens were length $l = 50$ mm, width $B = 10$ mm, thickness of adherends $t_{Al} = 3.175$ mm, and initial crack length $a_0 = 25$ mm. The three selected adhesive thicknesses, t_h, were 0.508 mm (20 mil), 1.524 mm (60 mil), and 3.048 mm (120 mil). A thin razorblade sprinkled with a diamond-lapping compound [17] was used to produce a V-notch at the initial crack tip. Each specimen was bonded individually. Figure 1(a) shows the geometry and 1(b) shows a photograph of a specimen.

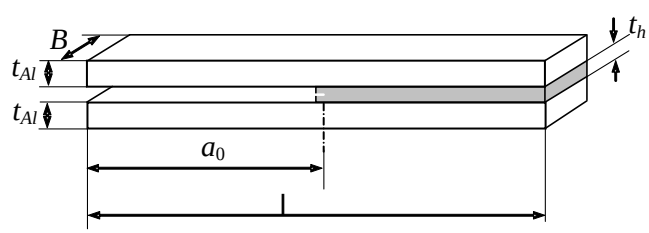

(a)

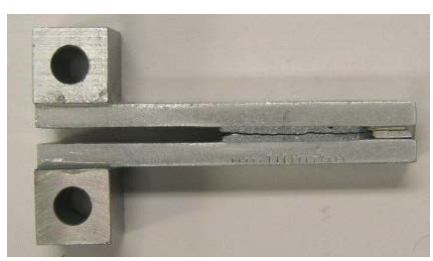

(b)

Figure 1. Specimen Group 1: (a) Specimen Geometry and (b) Actual Specimen

To consider the transferability of the material data obtained on specimen group 1, a second group of adhesively bonded specimens was fabricated. These specimens were produced and tested independently in a different laboratory. For group 2, the larger size DCB specimens were length l = 125 mm, width B = 17 mm, and thickness of adherends t_{Al} = 3.175 mm. Specimens in group 2 had an initial crack length of a_0 = 38 mm. Specimens with two adhesive thicknesses, t_h = 1.524 mm (60 mil) and 3.048 mm (120 mil), were tested. The initial crack was produced by a process slightly different from the process of group 1. Teflon® spacers with different specified thicknesses were attached to the inside surfaces of the adherends to control the adhesive layer thickness. Adhesive was applied onto the inside surfaces of the adherends with spacers. Before bonding, a very thin (0.02 mm) Teflon film was coated with mode release film and inserted along the midline of the adhesive layer to create the initial crack. Specimens with the same adhesive thickness were prepared by bonding two large aluminum panels. After curing, the specimens were cut into the required size using a water-jet. Piano hinges were attached to the opening end of the specimens after cutting. Before the test, all the spacers and the thin Teflon film were removed.

2.1.3 Test Procedures.

The group 1 DCB specimens were loaded in an electrodynamic test machine (ElectroForce® 3200, Bose® Corp—ElectroForce Systems Group, Minnetonka, MN, USA) under displacement control with a constant displacement rate of 0.001 mm/sec. Loading blocks glued to the aluminum adherends and frictionless pins were used to attach the specimen to the fixtures of the test frame. From the experimental records of force, F, and applied load-line displacement, v_{LL}, the energy release rate G was calculated. For the analysis of the crack growth, a digital image correlation (DIC) system, VIC-2D (Correlated Solutions, Inc., West Columbia, SC, USA), was used. The side surface of the DCB specimen was polished and covered with a speckle pattern by depositing a mist of white paint. A digital camera (Retiga 1300™, QImaging®, Burnaby, BC, Canada) with a charge-coupled device pixel size of 6.7 by 6.7 μm and a 1:1 magnification telecentric lens was used for image acquisition. Images of the specimens in the undeformed and subsequent deformed states at various stages of loading were captured. The camera was connected to a digital image capture board with a data acquisition system that recorded the force displacement and synchronized the image acquisition. Displacements fields (u and v) on the specimen surface were obtained from correlations between the speckle images for the undeformed and deformed states, respectively [16]. In particular, the crack tip-opening displacement at the initial crack tip (Δ_n^*) was extracted from the full-field displacement field and recorded. Figure 2 shows the experimental setup.

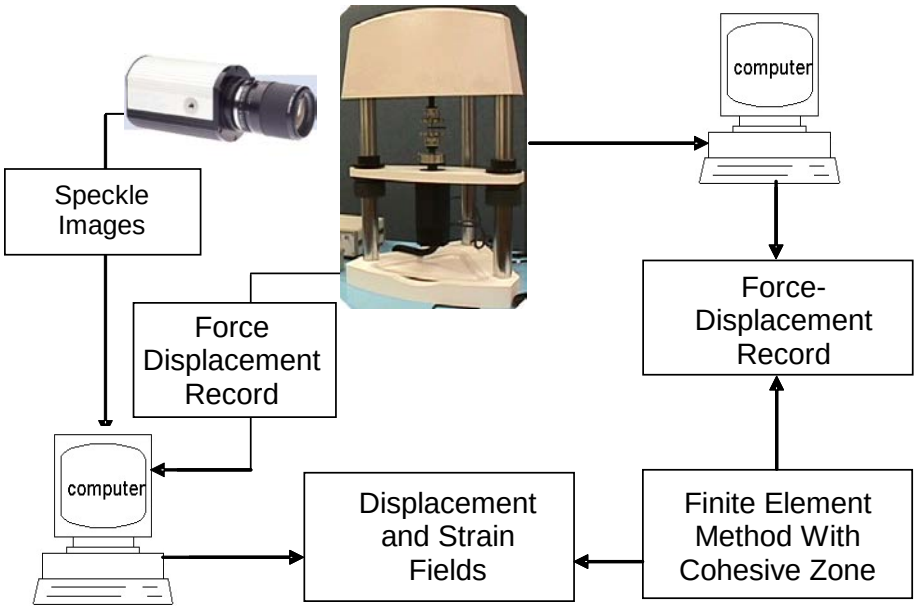

Figure 2. Experiment Setup

Experimental verification of the absence of plastic deformation in the adhesively bonded joint fracture process can be performed by matching the corresponding fracture surfaces to each other. This type of detailed experiment was conducted. Corresponding features were identified on corresponding fracture surfaces. The selected features were imaged using a stereo-imaging system. In particular, the present investigation used an optical image system with a compound microscope for which the specimen table was actuated by a stepper motor. Thus, the focal plane was moved through the three-dimensional (3D) surface, and a partially focused image was obtained for each position, each encoded with relevant height information. Using appropriate imaging software (Helicon Focus™, Heliconsoft®), individual image slices were stacked, and a 3D image was obtained. On these digital elevation models, height measurements were performed along paths linking corresponding features on opposing fracture surfaces. A commercial software package was used for the analysis (MeX, Alicona, Inc.).

The DCB specimens of group 2 were tested independently of group 1. A servohydraulic test system (MTS, Inc.) was used. Using the attached piano hinges, specimens were loaded under displacement control with a constant displacement rate of 0.005 mm/sec. During the specimen loading, digital images of the crack tip were taken through an optical microscope sitting on a moving frame. When the crack propagated, the microscope was moved to follow the new crack tip, and the digital camera took photographs of the crack tip region during the crack extension. The crack tip-opening angle (CTOA) was measured at a distance of 0.2 mm behind the crack tip and recorded together with the corresponding crack extension length. CTOA data were subsequently related to crack extension.

2.1.4 Analysis Methodology.

The DCB is considered a nonhomogeneous sandwich beam. The adhesive material was transformed to the material of the adherends by the ratio of the elastic moduli, $n = E_h/E_{Al}$. The equivalent moment of inertia, $\bar{I}$, for the sandwich beam was calculated by

$$\bar{I} = \frac{1}{12} b t_{Al}^3 + b t_{Al}\left(c - \frac{t_{Al}}{2}\right)^2 + \frac{1}{12} n b\left(\frac{t_h}{2}\right)^3 + \frac{1}{2} n b t_h\left(c - t_{Al} - \frac{t_h}{4}\right)^2 \tag{1}$$

$$c = \frac{1}{2}\left[t_{Al}^2 + t_{Al} t_h + n\left(\frac{t_h}{2}\right)^2\right] \Big/ \left(t_{Al} + n\frac{t_h}{2}\right)$$

Where geometric variables are defined in figure 1 and c is the distance from the neutral axis of the arm of the DCB to the top of the sandwich DCB specimen. Thus, with the equivalent moment of inertia, $\bar{I}$, and the elastic modulus of aluminum, E_{Al}, the energy release rate for the DCB specimen composed of the aluminum adherends and adhesive was calculated as [16]

$$G = \frac{F^2}{E_{Al}\bar{I}\, b}\left(\frac{3E_{Al}\bar{I}\cdot v_{LL}}{2F}\right)^{2/3} \tag{2}$$

where F is force and v_{LL} is applied load-line displacement

The cohesive zone law characterizes the processes at the crack tip during material separation in the form of a relationship between material separation and related tractions. The cohesive zone law is obtained by a differentiation of the curve of energy release rate, G, versus crack tip opening at the initial crack tip, Δ_n^* [16 and 18-20]

$$T_n = \frac{\partial G\left(\Delta_n^*\right)}{\partial \Delta_n^*} \tag{3}$$

From the resulting traction-separation curve, the cohesive strength, σ_{max}, was extracted as the peak traction value, and the cohesive energy, ϕ, as the area under the traction-separation curve. The cohesive energy, ϕ, is equal to the critical value of the energy release rate at crack initiation.

2.1.5 Model Implementation.

Numerical simulations of the crack growth experiments were performed by using the finite element method and cohesive zone elements for crack growth simulation. Figure 3(a) shows the model geometry and boundary conditions, and figure 3(b) shows a typical finite element mesh. The adhesive bondline thickness considered in the simulations was t = 1.524 mm. The CZM was embedded in cohesive elements placed along a straight line in front of the initial crack tip. Due to the symmetry of the specimen relative to the center plane, only half the DCB specimen was

modeled. For specimen group 1, both the two-dimensional (2D) plane-strain conditions (for the analysis of the overall specimen response) and the 3D conditions (for the detailed analysis of the crack tip conditions) were considered; for specimen group 2, only plane-strain analysis was conducted. In the 2D plane-strain condition, the solid elements were four-node bilinear plane-strain elements with a rectangular shape. The cohesive zone elements used in the 2D study possess four nodes and two integration points. In the 3D condition, the solid elements were eight-node linear elements. The corresponding 3D cohesive elements possessed eight nodes and four integration points. Computations were performed with the commercial finite element code ABAQUS® (ABAQUS, Version 6.1), for which the cohesive elements were implemented using the user-defined subroutine UEL.

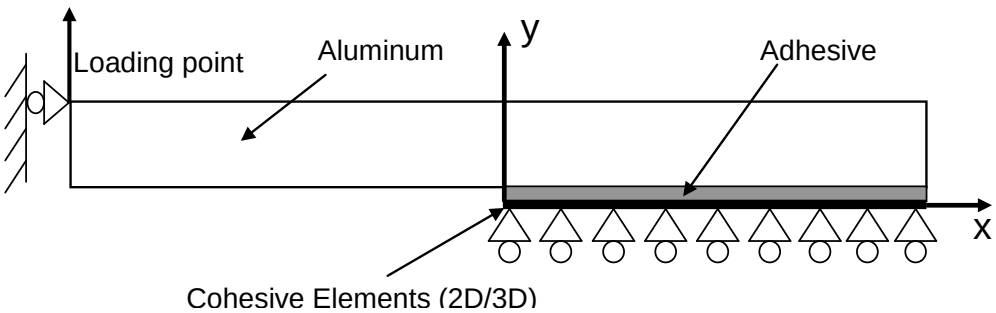

(a)

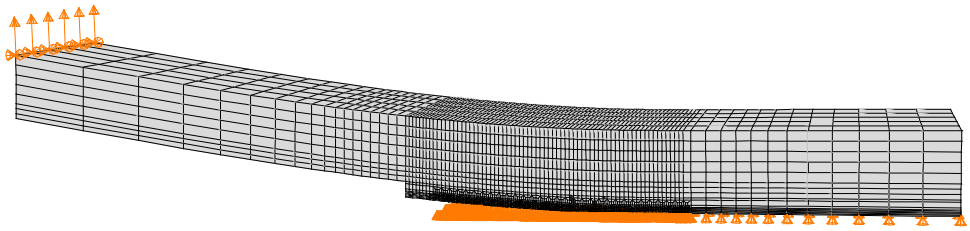

(b)

Figure 3. (a) Model Geometry and (b) Representative 3D Finite Element Mesh for Specimen Group 1

2.2 RESULTS ON DCB SPECIMENS UNDER QUASISTATIC LOADING.

2.2.1 Load Displacement Records.

Experimental results on two replicates of group 1 for bondline thicknesses, 0.508, 1.524, and 3.048 mm, are given in the form of force versus applied load-line displacement (F-v_{LL}), figure 4(a). Furthermore, figure 4(b) shows the crack extension, Δa, versus the applied load-line displacement (Δa-v_{LL}) from those samples for which the crack extension data was observed. In all the experiments, the F-v_{LL} curve is linearly increasing until the peak load, which is between 200 and 220 Newtons (N). After the peak load, the load drops slowly with the crack propagation. The F-v_{LL} curves for different bondline thicknesses show similar behavior. However, after the peak load, the F-v_{LL} data shows moderate variability between individual specimens.

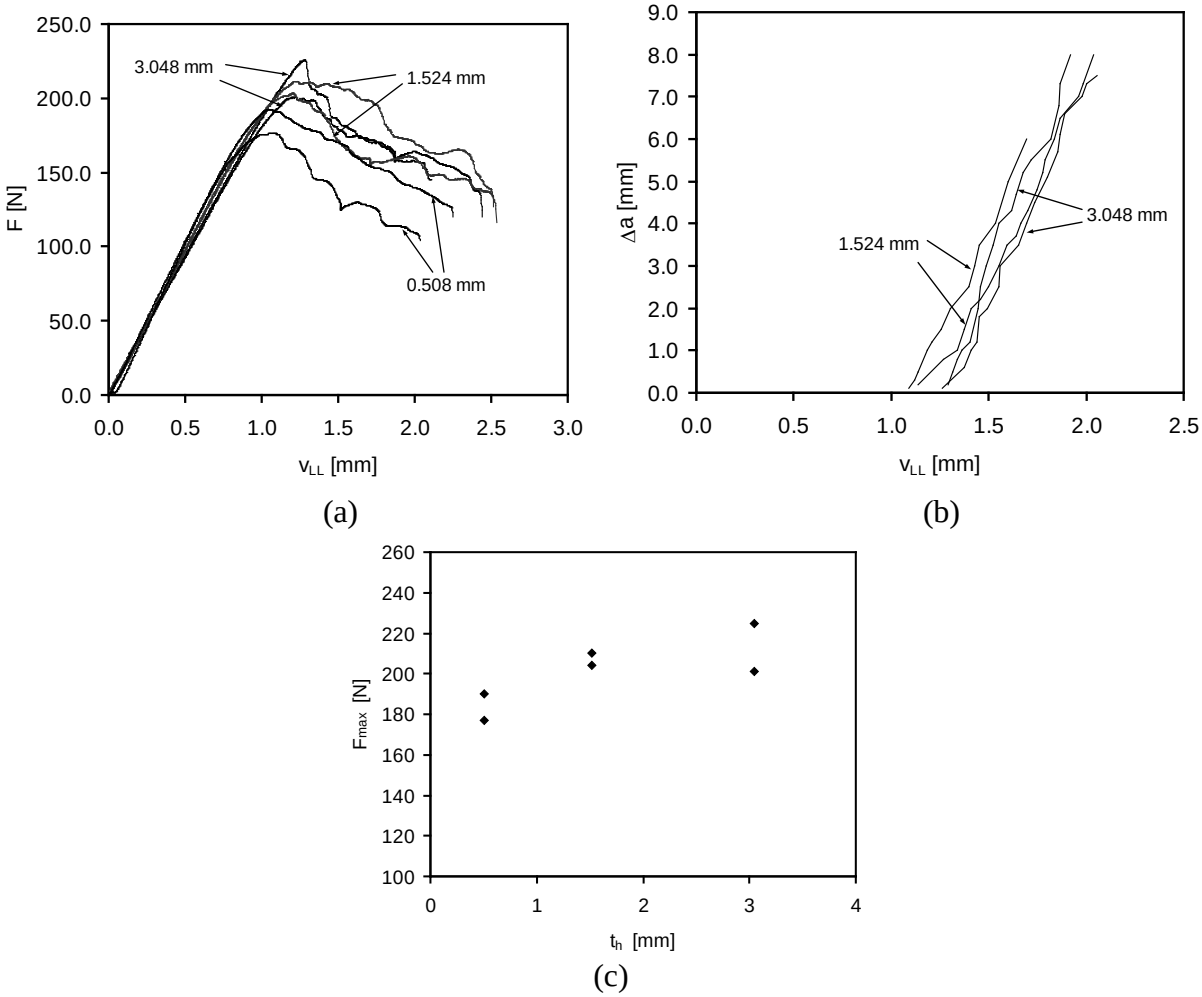

Figure 4. Experimental Results of Specimen Group 1

The variability was not large enough to differentiate dependence of the measured failure load on the bondline thickness [1 and 2], especially for the specimens with two thicker bondline thicknesses. The dependence of the peak loads on the bondline thickness is shown in figure 4(c). The peak loads of the adhesive for the two thicker bondline thicknesses (1.524 and 3.048 mm) were more than 220 N. Nevertheless, the peak loads were slightly lower for the specimen with t_h = 0.508 mm due to the tendency of adhesion failure. This adhesion failure tendency was clearly observed in the fracture surface of the specimen with different bondline thicknesses (figure 5). It is evident that the 1.524- and 3.048-mm-thick specimens show the perfect cohesive failure. However, the 0.508-mm specimen (thin bondline thickness) showed the tendency to fail in adhesion.

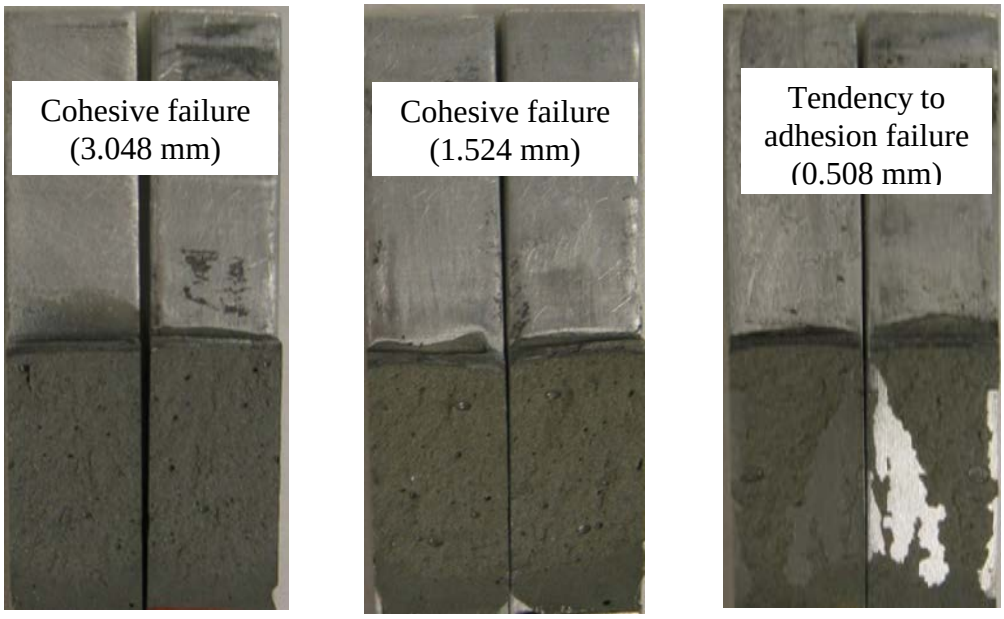

Figure 5. Fracture Surfaces of Specimen Group 1

When comparing figure 4(a) and (b), it is evident that the reduction of the loads in the F-v_{LL} curves coincides with the initiation of crack growth after peak loads. The observed crack extension curves for the specimen with cohesive failure (bondline thicknesses 1.524 and 3.048 mm) showed the same type of behavior. At the beginning, in the crack initiation region, the crack growth rate was slower than the crack growth rate after 1- to 2-mm crack extension. Then, the crack grew at a relatively stable crack growth rate. Crack extension showed discontinuity corresponding to the experimental F-v_{LL} behavior, which was not completely smooth. The average crack extension rates for all the samples with different bondline thicknesses after the crack initiation region were observed to be nearly identical.

2.2.2 Validity of a Nonlinear-Elastic Analysis Approach to Joint Failure.

For the nonlinear-elastic analysis approach to be valid, the contribution of any irreversible deformation needs to be excluded. To estimate the contribution of irreversible deformation of the adhesive to joint toughness, the adhesive was assumed to deform as an elastic-plastic material. (Typical parameters for yield strength and hardening of Hysol EA-9394 are given in table 1.) To estimate the contribution of plastic dissipation to toughness, the size of a reference plastic zone, R_0, is defined as [12 and 21]

$$R_0 = \frac{2}{3\pi(1-\eta^2)}\left[\frac{(1-\nu_h^2)}{E_h} + \frac{(1-\nu_{Al}^2)}{E_{Al}}\right]^{-1} \frac{\phi}{\sigma_{y,h}^2} \tag{4}$$

where η is the second Dundurs' parameter and ν_h and ν_{Al} are Poisson's ratios for the adhesive and aluminum, respectively.

$$\eta = \frac{1}{2\mu_h} \frac{\mu_h(1-2\nu_{Al}) - \mu_{Al}(1-2\nu_h)}{(1-\nu_{Al})\mu_h + (1-\nu_h)\mu_{Al}} \tag{5}$$

where μ_h and μ_{Al} are the shear moduli of the adhesive and the aluminum adherends. The ratio of bondline thickness to the reference plastic zone size, t_h/R_0, can be used to estimate the potential contribution of plasticity to toughness. For the present study, the values of t_h/R_0 equal to 1.0 and 2.0 were used for the bondline thickness values of t_h = 1.524 mm and t_h = 3.048 mm, respectively. The results of references 12 and 21 demonstrated that within the range of t_h/R_0 values, the effect of the plasticity on joint toughness was small. Furthermore, the contribution of plasticity to toughness strongly depends on the material hardening. The results of references 11, 22, and 23 indicate that materials with stronger material hardening showed a much less pronounced *R*-curve behavior than those with low hardening (all other plasticity conditions being the same).

For the material studied, as shown in table 1, the hardening modulus is about half the elastic modulus. Based on the value of t_h/R_0 and high hardening behavior in the plastic regime, it is estimated that the contribution of plastic deformation to the joint toughness can be negligible, and an elastic analysis of the joint is justified. If such crack paths lead to matching surfaces, then the absence of plastic deformation during crack growth is demonstrated. Figure 6(a) shows planar images of corresponding fracture surfaces of the adhesively bonded joints investigated. Corresponding crack paths on the opposing crack surfaces are indicated and are used to define two paths from the initial crack tip along the crack growth direction. Once the height information along these paths was extracted, the two paths were placed relative to each other. Figure 6(b) shows this result. This figure indicates that the two fracture surfaces match well to each other, indicating the absence of significant amounts of plastic deformation during joint failure. This finding justifies using the determination of the traction-separation law from the measurement of the energy release rate and local crack tip deformation, as outlined in the following section.

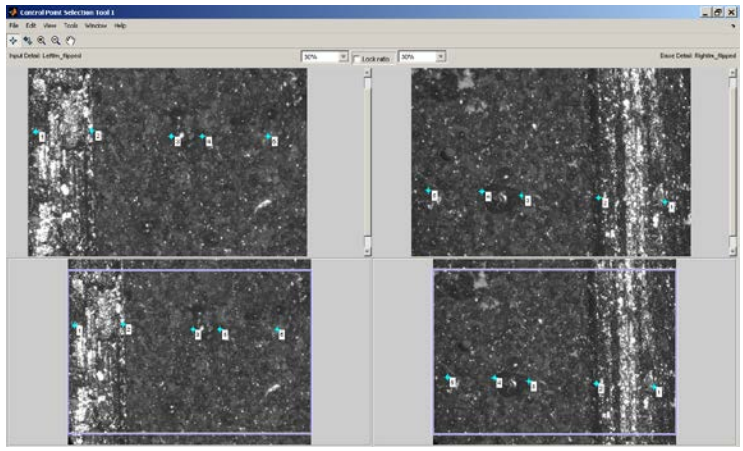

(a)

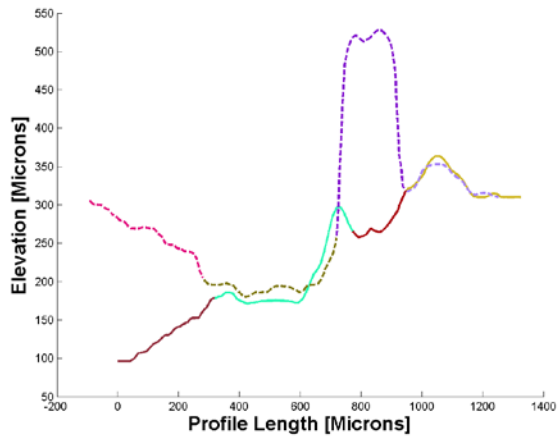

(b)

Figure 6. (a) Surface Images and (b) Fracture Reconstruction

2.2.3 Determination of Cohesive Zone Law.

Figure 7(a) shows a plot of energy release rate versus crack-opening displacement at the original crack tip, Δ_n^*, for three bondline thicknesses: 0.508, 1.524, and 3.048 mm. The values of Δ_n^* were determined using the DIC. All experimental data sets for different bondline thicknesses show the same tendency: at the beginning, the energy release rate value increases with the increase of the opening, and later reaches a steady state. The corresponding plot of the differentiation from the data in figure 7(a) is shown in figure 7(b), the traction-separation law obtained for the three adhesive thickness values. The cohesive zone law was found to be quite independent of the adhesive layer thickness. It is characterized by a maximum traction value, i.e., the cohesive strength of approximately 80 MPa. The cohesive energy, i.e., the area under the traction-separation curve, was determined to be 1.4 N/mm for the 1.524- and 3.048-mm-thick specimens. For the 0.508-mm-thick specimen with a tendency to adhesion failure, the cohesive energy was found to be less, i.e., 1.2 N/mm. This also corresponds to F-v_{LL} curve behavior, in which the curve for the 0.508-mm-thick specimen is lower than those specimens with larger thicknesses.

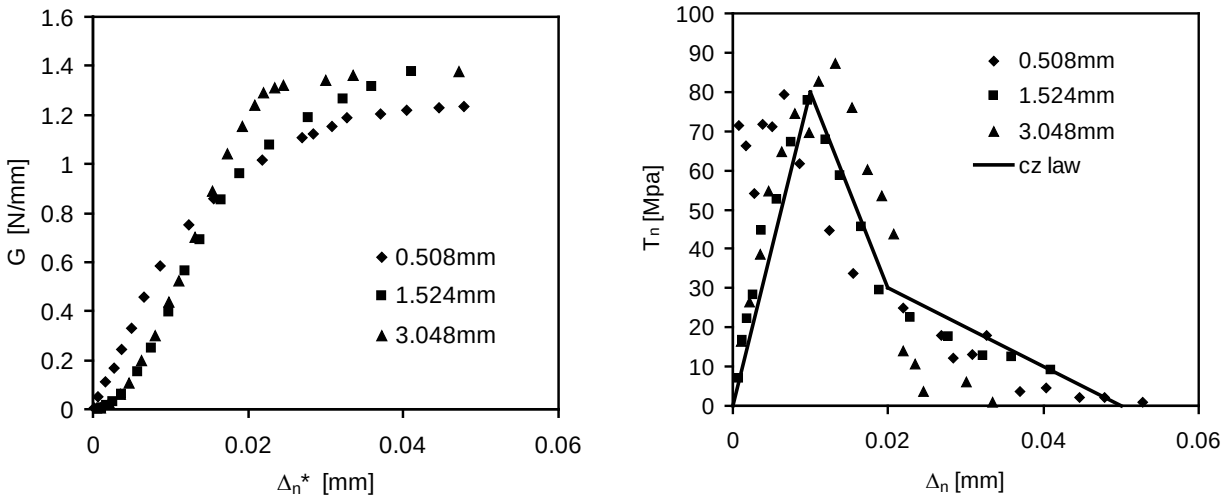

(a) (b)

CZ = Cohesive zone law

Figure 7. Determination of Cohesive Traction-Separation Law for the Adhesive

Based on experimental data, it is shown that crack growth resistance for the Hysol EA 9394 adhesive is independent of adhesive thickness under the condition that failure is cohesive. The trilinear cohesive zone law is in the following form

$$T_n = \begin{cases} \dfrac{\sigma_{\max}}{\beta\delta}\Delta_n & \Delta_n \le \beta\delta \\ \sigma_{\max} - \dfrac{\sigma_{\max} - \bar{\sigma}}{(\beta-\gamma)\delta}(\beta\delta - \Delta_n) & \Delta_n \le \gamma\delta \\ \bar{\sigma}\dfrac{\delta - \Delta_n}{(1\gamma - \delta)} & \Delta_n > \gamma\delta \end{cases} \tag{6}$$

with σ_{max} as the cohesive strength, i.e., the maximum traction value; δ as the cohesive length; and β, γ as the shape factor to specify the split point in the trilinear function. The cohesive energy is $\phi = (\gamma\sigma_{\max}\delta + \bar{\sigma}\delta - \beta\bar{\sigma}\delta)/2$. The traction reaches the peak value, σ_{max}, at the separation $\Delta_n = \beta\delta$. σ is the traction at a separation of $\Delta_n = \gamma\delta$. To determine the trilinear data fit, the entire set of $T_n - \Delta_n$ data is separated into three parts by assuming a trial value for β, γ. Then, for each data subset, a linear regression analysis was conducted. This process was iterated such that the two intersects of the three linear regression functions were located at the selected $\Delta_n = \gamma\delta$ and $\Delta_n = \beta\delta$. Following this process, the cohesive zone parameters were obtained as σ_{max} = 80.0 MPa; δ = 0.05 mm; β = 0.2; γ = 0.4; σ = 30.0 MPa, with σ_{max} the effective cohesive strength, i.e., the maximum traction value; and δ the cohesive length. The cohesive energy was $\phi = (\gamma\sigma_{max}\delta + \bar{\sigma}\delta)/2$.

2.2.4 Simulation Results.

The simulation results of both the 2D plane-strain and the 3D models for the global specimen behavior calculated with the cohesive zone law obtained from experiments are included together with the experimental data in figure 8. Initially, the predicted F-v_{LL} curve increased linearly until the peak load. Beyond that, the force decreased with the applied displacement because of the extension of the crack. The simulation results of the 2D and 3D models were quite similar except that the peak load from the 2D simulation was slightly larger than the 3D simulation. Also, the peak load for the 2D simulation occurred slightly earlier than the 3D simulation results. Moreover, the simulation results from both the 2D and 3D models were in good agreement with the experimental results. Both initial parts before crack extension and the predicted peak loads matched the experiment measurements well. The predicted initial slopes matched the slopes observed from the experiments very well. The predicted peak loads, depending mainly on the cohesive energy [15], were in the range of the experimentally obtained values at the crack initiation. This shows the cohesive zone law obtained from the experiments is capable of capturing the material behavior of this type of adhesive. In the simulated F-v_{LL} curves from both 2D and 3D models, the decaying parts after the peak load were nearly identical and fell within the average range of the experimental data.

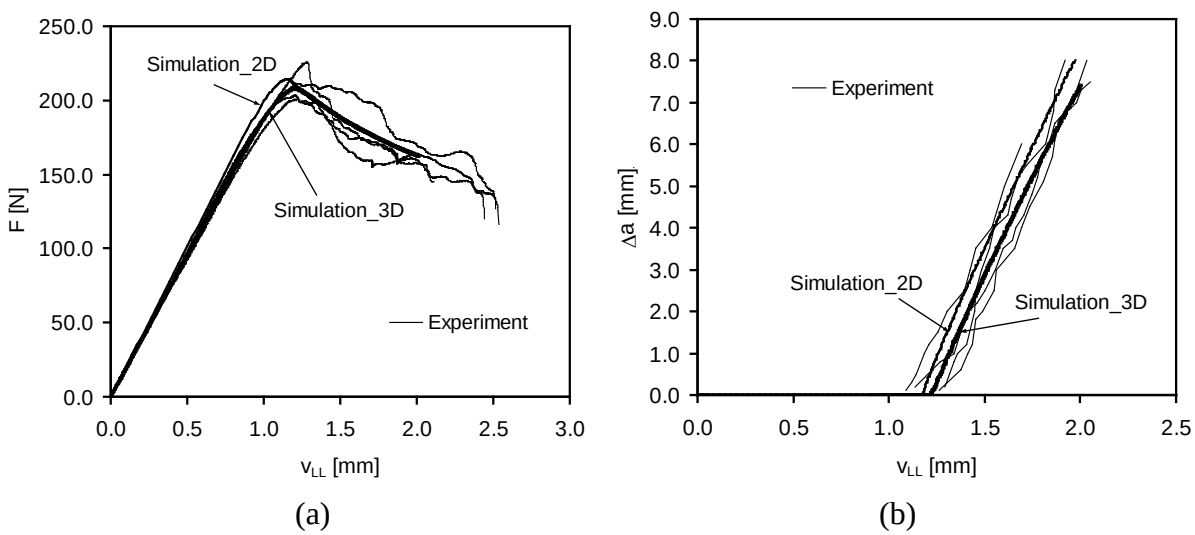

Figure 8. Comparison of Finite Element Simulation Results and Experimental Data for Specimen Group 1: (a) Force Deflection Response and (b) Crack Extension

The simulations also allowed for tracking the crack growth. The crack growth data from both the 2D and 3D simulations were plotted together with the experimentally obtained data, as shown in figure 8(b). The crack extension for the 3D model is on the side surface of the model. The tip of the crack is defined as the separation equal to the cohesive length. The initiation point from the 2D simulation occurred slightly earlier than the 3D simulation. This coincides with the F-v_{LL} curve behavior, in which the peak load occurred earlier in the 2D simulation than in the 3D simulation. However, the predicted initiation point was within the range of the applied displacement value obtained from experiments, i.e., between 1.1 and 1.3 mm. The predicted

crack growth rates from the 2D and 3D simulations were nearly identical. Moreover, this simulated crack growth rate was exactly the same as the average crack growth rate observed from the experiments at the steady crack growth region. In summary, the crack growth simulations are in very good agreement with the experimental measurements.

2.2.5 Strain Fields Near the Crack Tip and Crack Opening.

Force load-line displacement records (F-v_{LL}) and crack extension data represent the global specimen behavior. The question remains how accurately the computations predict the local deformation behavior of the strain fields at the crack tip during crack growth. The analysis proposed here allows investigation into this aspect.

The experimentally determined strain distribution of ε_{yy} in front of the crack is given in figure 9(a). The contour plot is nearly symmetrical due to the symmetry condition of the DCB loading test. The strain distribution clearly shows strain concentration with the peak value of the strain presented at the crack tip. It is also evident that the area of large strain was confined mainly to the adhesive layer. The strain in the region outside the adhesive layer was very small compared to the strain in the adhesive layer. This is because the elastic modulus of the adhesive was much smaller than the aluminum adherends, which caused the deformation that occurred in the adhesive layer to be much larger than in the aluminum adherends.

Figure 9(b)-(d) shows the strain distribution fields from the 2D and 3D models, respectively. Figure 9(b) is the computation results from the 2D model. From the comparison, it is evident that the 2D simulation did not compare very well with the experimental-measured strain field, despite the fact that the crack growth behavior was well approximated. Much better agreement was obtained between experiment and simulation in the surface 3D model case, figure 9(c). Both the strain value and the contour shape were predicted well. The characterization of the strain constrained in the adhesive layer is also shown very clearly. Figure 9(d) shows the strain computation on the mid-plane of the specimen from the 3D model. First, it is evident that the strain value of the mid-plane and the surface were very different. Second, by comparing figure 9(b) and (d), it is clearly shown that the strain field in mid-plane is similar to the strain field computation from the 2D model. This verifies that the condition of the mid-plane in the 3D model was actually close to the 2D model.

In conclusion, the 2D model can only approximate the basic strain concentration behavior; the value and shape were not predicted very well. Computation of strain distribution on the surface from the 3D model was in good agreement with the experiment measurements for both values and shapes by using the cohesive zone approach. The strain field calculation of the mid-plane from the 3D model is similar to the calculation from the 2D model.

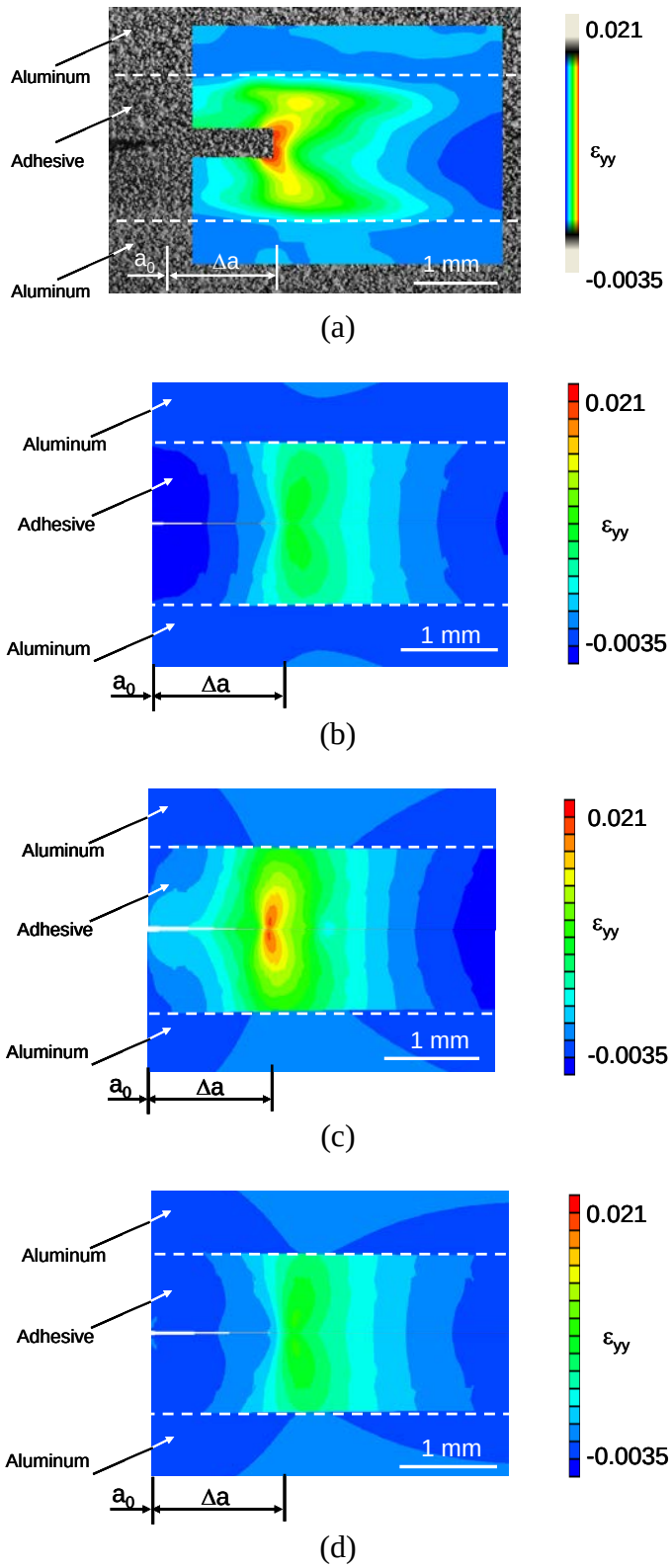

Figure 9. Strain Field Comparison: (a) Strain Field From Experiments, (b) Strain Field Computation of the 2D Model, (c) Strain Field Computation of Side Surface From the 3D Model, and (d) Strain Field Computation of Mid-Plane From the 3D Model

Figure 10 depicts crack tip-opening displacement at the initial crack tip, Δ_n^*, versus load-line displacement for both the 2D and 3D simulation results. For the 3D simulation, both crack-opening displacements on the surface and on the plane close to the mid-plane are illustrated in figure 10. The prediction from the plane close to the mid-plane is actually the crack-opening displacement calculation on the plane with a 1-mm distance from the mid-plane due to the absence of the nodes at the mid-plane on the current 3D model. Clearly, there is a difference between the 2D and 3D simulations. The 3D simulation results close to the mid-plane were close to the 2D simulation results. This further verified that the condition in the middle of the 3D model was close to the 2D plane-strain condition. The 3D simulation results on the surface were smaller than the 2D simulation results. During the experiments, only the crack-opening displacements on the surface were accessible and could be used to determine the cohesive zone law.

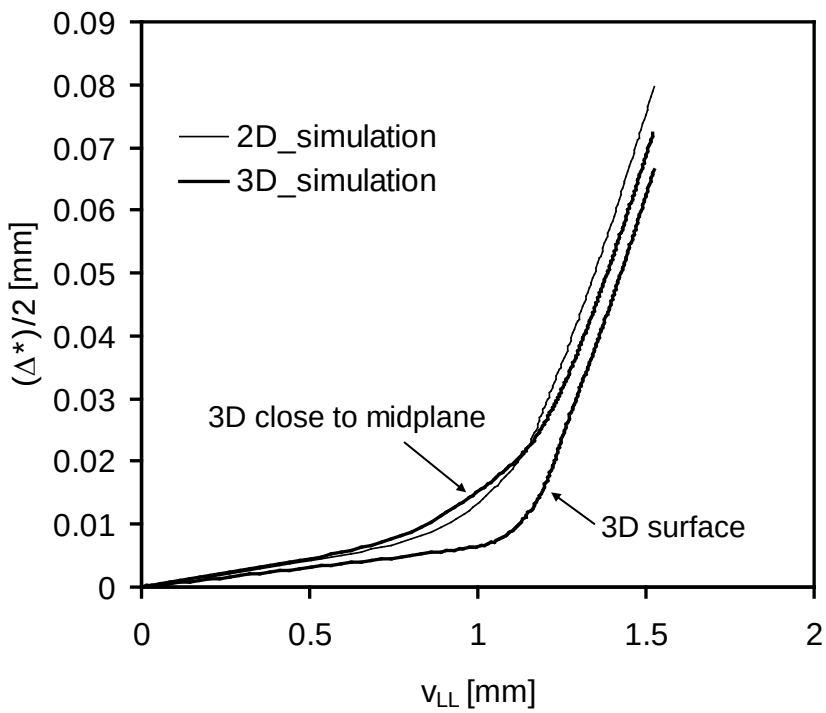

Figure 10. Predicted Crack Tip-Opening Displacements in the Plane-Strain and 3D Simulations

At small, load-line displacements, the crack-opening displacements on the surface were similar to the crack-opening displacements close to the mid-plane. This shows that the cohesive strength was not significantly affected by the effect of the crack tip-opening displacement since cohesive strength was determined at the small crack tip opening. With the crack tip opening further increasing, the difference of Δ_n^* between the surface and the inside plane becomes larger. This could affect the softening parts of the cohesive law, which is unavoidable. Nevertheless, the traction was reduced during the softening parts, especially at the end of the traction-separation law. Although the difference of Δ_n^* becomes larger, the effect to the entire cohesive law would be small.

2.2.6 Transferability of Crack Growth Characterization.

The cohesive zone law obtained from the DCB specimens captured both the global crack growth behavior and the local strain field at the crack tip region. Next, the cohesive zone law obtained from those experiments was applied to simulate the experiments conducted on specimens of different geometry. This was done to verify the transferability and geometry independence of the experimentally obtained cohesive zone law. If the cohesive zone law is found to be applicable to the larger specimens, it will confirm that the cohesive zone parameters can be considered material parameters and, hence, are applicable to different geometry and loading configurations.

Thus, the transferability of the cohesive zone law approach was investigated by applying simulations with the CZM to joint configurations other than that from which the cohesive zone law was measured. The DCB specimen geometry (initial crack length a_0 = 38 mm, width B = 17 mm, thickness of adherends t_{Al} = 3.175 mm, and length l = 125 mm) used to verify the transferability was different from the DCB specimen used to obtain the cohesive law (a_0 = 25 mm, B = 10 mm, t_{Al} = 3.175 mm, and l = 50 mm). Here, the specimen (B = 17 mm) used to verify the transferability was referred to as the "large specimen," and the specimen (B = 10 mm) used to obtain the cohesive law was referred to as the "small specimen."

The simulation considered here was the 2D plane-strain model with a 1.524-mm bondline thickness adhesive layer. The finite element model of the large specimen was established by using the cohesive zone law obtained from the small specimen. The boundary and loading conditions of the finite element model used in the simulation was the same as described in section 2.1.5. The simulation results of the global F-v_{LL} curve calculated with the cohesive zone law obtained from the small specimens are included together with the experimental data in figure 11. The experiment data included two different bondline thicknesses, 1.524 and 3.048 mm. The F-v_{LL} curves for the two thicknesses showed the same type of behavior with the same initial slope and approximately the same peak loads. This is similar to what was observed in the small specimen experiments. From the good prediction of the force versus load-line displacement by using the cohesive zone law obtained from specimens with different geometries, it is clearly shown that the cohesive zone law is geometry-independent and transferable for this type of adhesive. By using the methodology described in this report, the cohesive zone law obtained by one type of experiment configuration can be used by another similar type, but scaled, geometry configuration. Thus, the cohesive parameter of the adhesive obtained from these experiments can be considered a material property and can be used to characterize the material behavior for the same type of material and loading condition.

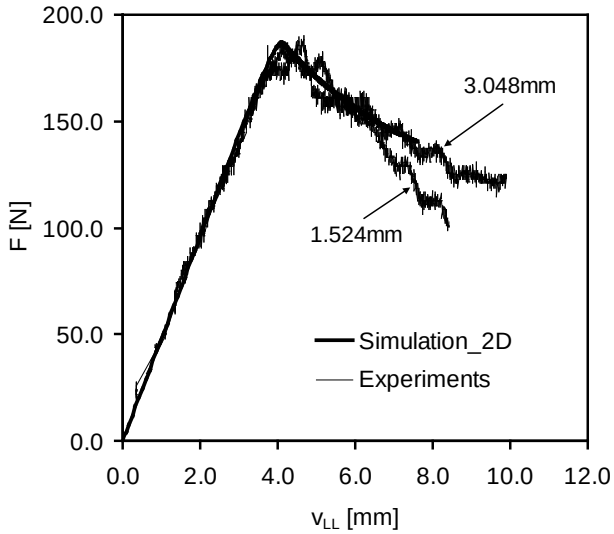

Figure 11. Comparison of Finite Element Simulation Results and Experimental Data Force Deflection Response, Specimen Group 2

2.2.7 Measurement and Prediction of the CTOA.

The CTOA was measured within 0.2 mm of the crack tip for the specimens with bondline thicknesses of 1.524 and 3.048 mm. In the finite element calculations, CTOA was obtained by first determining the location of the current peak of the tractions, then the separation was calculated at a distance of 0.2 mm behind this location, and the angle was then computed as $CTOA = 2 \times \arctan[(\Delta_n^* /2)/0.2]$.

Figure 12 shows the CTOA prediction from the 2D model (for both the small and large specimens) and the 3D model (for the small specimen) as well as the experimental-measured CTOA. It is shown that the prediction of CTOA evolution from the 2D and 3D models on the surface showed the same trend as the experimental-measured CTOA data. The values of CTOA were large at the crack initiation region but decreased substantially within the first 1-mm crack extension transient region. After that, a plateau of CTOA value was reached during the steady-state crack growth region. The constant CTOA value can be considered as the critical value when evaluating the failure process of the material. A similar CTOA trend was also found by evaluating the crack growth of other types of materials [24].

From the 2D model calculation for both small and large specimens, the CTOA value at initiation is 6.3°, which is larger than the steady-state CTOA value, 5.25°. The prediction of CTOA from the 3D model surface showed the same trends with the 2D model, but with slightly larger values. The predicted CTOA value from the 3D model surface at initiation was 7.7º, and the steady-state CTOA value was 6.0º. This is because the opening at the surface was larger than in the mid-plane, which is constrained and more like the plane-strain condition. The 3D model prediction, other than on the surface (shown on figure 12 as “Simulation_3D_close to mid-plane”) is actually the calculation of CTOA at the plane with a 1-mm distance from the mid-plane due to the absence of the nodes in the mid-plane on the current 3D model. At the beginning, this

prediction was close to the 2D model; after about a 2-mm crack extension, the value of CTOA was equal to the 3D model prediction on the surface when the crack extension reached steady state.

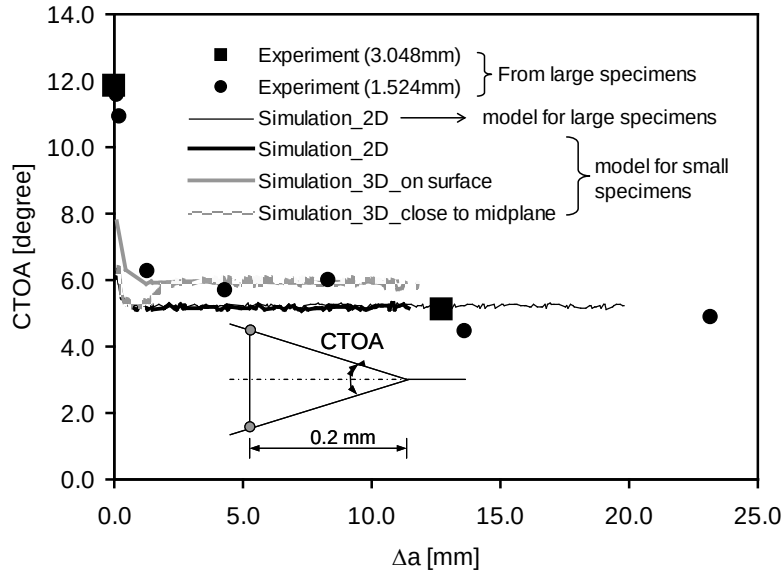

Figure 12. Experimental Data on CTOA and Finite Element Predictions

In the steady state, the predicted CTOA values from both the 2D and 3D models are within the average of the experimental-measured CTOA values, although the 3D prediction was slightly higher than the 2D prediction. The good agreement of the local CTOA behavior between the simulation and the experiments further verifies the success and feasibility of the transferability of the cohesive zone law. Additionally, for the 2D model, the predicted CTOA values from the small and the large specimens gave nearly identical results, as shown in figure 12. This validates that the CTOA criterion for this type of adhesive is not affected by the geometry of the specimens to evaluate the failure process of the adhesively bonded joints for the condition considered, where the plasticity of the adhesive is considerably small or negligible.

3. MIXED-MODE LOADING.

3.1 ANALYSIS APPROACH.

3.1.1 The Extended Finite Element Method.

The XFEM solves the problem of crack path selection during a crack propagation analysis [7 and 8]. Conventional finite elements are enriched with a particular set of shape functions. These shape functions are activated by a strength criterion, and once activated, they effectively allow for an element to be split into parts with one part on either side of the newly inserted crack. Several references in the recent literature describe the details of the method. The present study used the implementation of the extended finite element method as available in ABAQUS.

3.1.2 Model Definition.

The analysis of the mixed-mode initiation toughness of adhesively bonded joints used a submodel of the overall adhesively bonded joint, figure 13. This submodel captured the crack tip region of the joint, including the adhesive and the adherends. The loading conditions applied to DCB, MMB (with a 50% mode mixity), and ENF specimens were substituted by respective displacement boundary conditions on the tip region submodel.

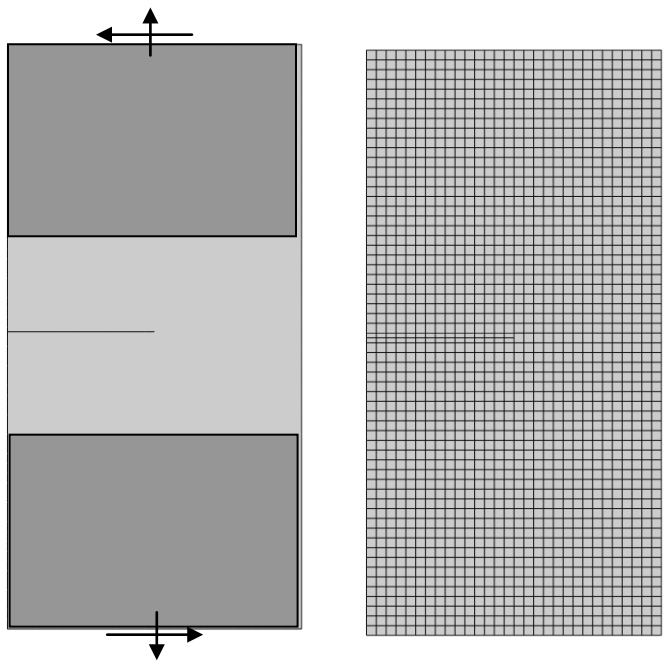

Figure 13. The Crack Tip Region of the Joint Submodel

The submodel was loaded by applying displacement boundary conditions. The applied displacements were for mode I loading, $U_x = 0$; for mode II loading, $U_y = 0$; and for mixed-mode loading, $U_x = U_y$. Thus, the mode mixity angles were 0°, 45°, and 90°. In the model, all elements belonging to the model domain of the adhesive were enriched such that crack propagation from the initial crack could proceed along any path without constraints imposed by the model. The crack propagation condition was such that enrichment was activated once the maximum principal stress reached the cohesive strength of the adhesive. The crack was then inserted into the model perpendicular to the direction of the maximum principal stress. Crack propagation followed subsequently with the material separation given by the traction-separation law of the adhesive.

3.2 RESULTS ON MIXED-MODE TOUGHNESS.

Computations of crack initiation in adhesively bonded joints loaded under mixed-mode conditions were conducted for five different joint thickness values, ranging from t_h = 6 mm to t_h = 0.3 mm. Loading was monotonic and proportional. For each adhesive thickness value and mode mixity, the angle of the growth crack emerging from the initial crack was determined from

the finite element simulation. Crack growth along a computed crack path leads to the dissipation of the cohesive energy as determined in the experiment on the DCB specimens. However, the analysis models for adhesively bonded joints assumed that crack growth occurred along a straight extension of the initial crack. For both cases, the same amount of energy has to be dissipated. Thus, an equation relating the crack path angle, the cohesive energy, and the mixed-mode fracture toughness can be developed

$$A \cdot \Gamma = A_x \Gamma_{mm} \tag{7}$$

where A is the true crack surface area along the actual crack path, A_x is the projection in the midline of the adhesive, Γ is the cohesive zone energy, and Γ_{mm} is the predicted mixed-mode toughness. The relationship between A and A_x is given as $A_x = A\cos\theta$, with the angle θ between the initial crack extension direction in mode I and the actual crack extension direction under mixed-mode loading. Then, the mixed-mode toughness is

$$\Gamma_{mm} = \frac{\Gamma}{\cos\theta} \tag{8}$$

From the finite element computations using the XFEM method, the angle of crack path deflection was dependent on the mode mixity and adhesive thickness. Γ was obtained as the fracture toughness of the adhesive, figure 14. For a linear elastic solid and the absence of any constraint, a reference solution is given at a crack angle of 70° when loading approaches mode II for a model considering the adhesive only. As a consequence, the mode II fracture toughness was predicted to be 1.6 times greater than the mode I toughness. The model also predicted that for moderate mode mixities (up to 50%), the increase in fracture toughness is small. Both findings are in good qualitative agreement with those obtained experimentally. Figure 15 shows the details of a crack tip for a mode II-loaded adhesive specimen. This experimental data compared well to the simulation shown in figure 16. For the mode II loading, the mode II toughness depended on the adhesive thickness, in that a reduced adhesive thickness led to reduced mixed-mode toughness through a reduced crack deflection angle. This finding is, again, in qualitative agreement with published experimental results. Figure 16 shows the deformed configuration for two adhesive thicknesses.

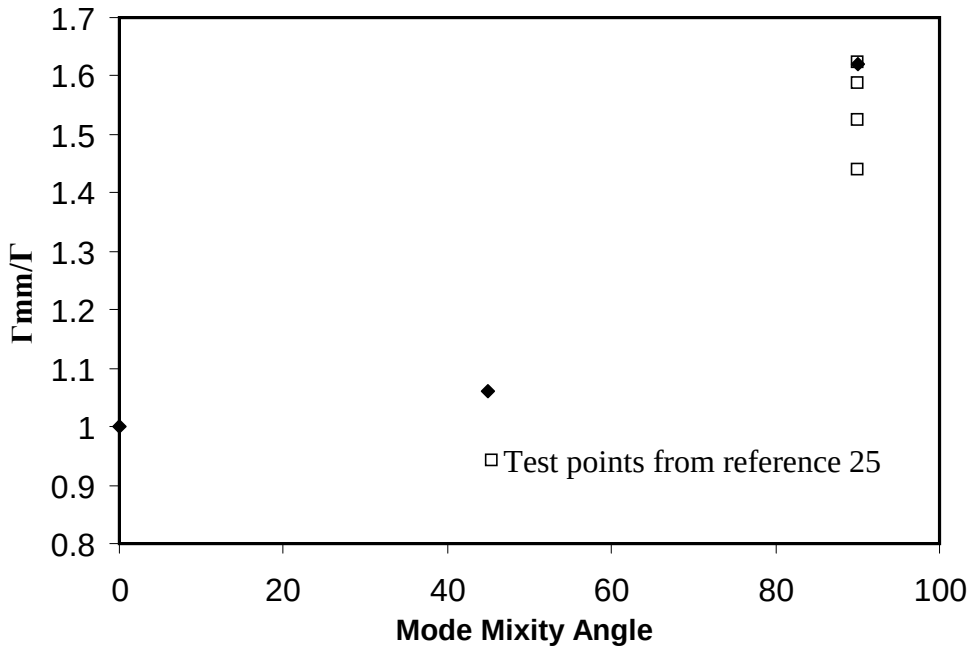

Figure 14. Predicted Mixed-Mode Toughness of Adhesively Bonded Joints

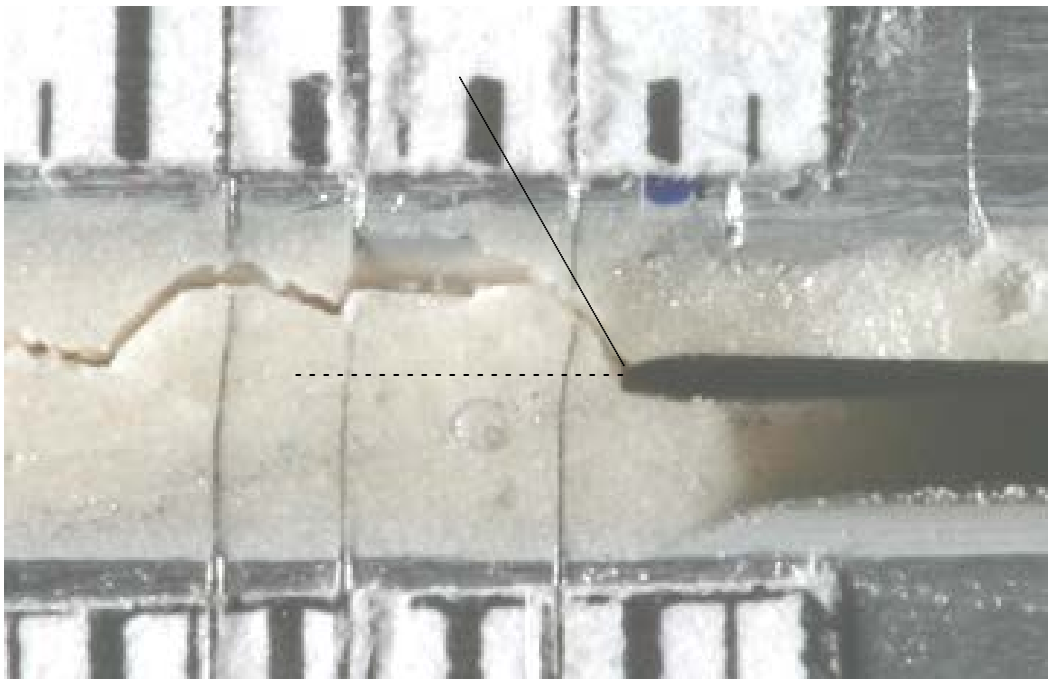

Figure 15. Crack Tip and Crack Path in an Adhesively Bonded Joint Loaded Under Mode II Conditions [25]

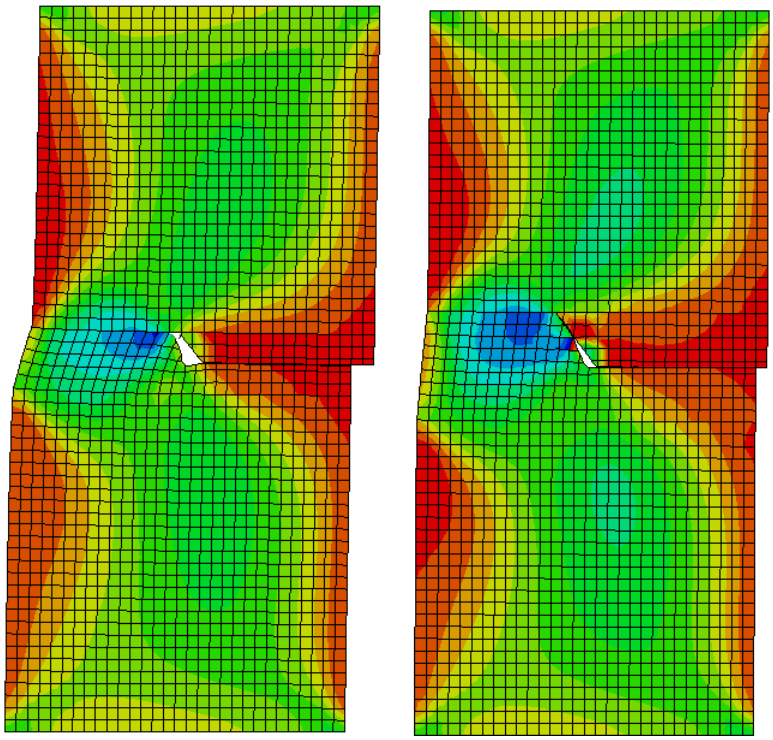

(a) (b)

Figure 16. Simulated Crack Paths Under Mode II Loading: (a) Thin Bondline and (b) Thick Bondline

4. CONCLUSIONS.

Crack growth was studied in Hysol® EA-9394™ structural adhesive. Double cantilever beam (DCB) specimens made of aluminum adherends and adhesive were used. The effect of variable adhesive bondline thickness on the failure of bonded samples was investigated. Based on the experimental data, it was shown that crack growth resistance for the Hysol EA 9394 adhesive is not strongly dependent on the adhesive bondline thickness under cohesion failure conditions. Both the global behavior (F-v_{LL} and Δa-Γv_{LL} curve) and the local behavior (strain field) were obtained experimentally. A numerical investigation of crack growth was conducted using an experimentally determined cohesive zone law. Both the two-dimensional (2D) plane-strain model and the three-dimensional (3D) model were simulated to compare with the experimental results in both global behavior (F-v_{LL} and Δa-v_{LL} curve) and the local behavior (strain field). It was found that both the 2D and 3D simulations predicted the global specimen response (F-v_{LL} and Δa-v_{LL} curve) well. However, for the local strain field, only the 3D simulation results on the surface were in good agreement with the strain field obtained from the experiment.

Furthermore, special attention was paid to the transferability (i.e., application to joint configurations other than that from which cohesive zone law was measured) and geometry independence of the cohesive zone model approach in this study. The cohesive zone law obtained from experiments was very successful at simulating the experimental results from geometry configurations other than that from which the cohesive zone law was measured. The

simulation results of both global force load-line displacement and local crack tip-opening angle (CTOA) behavior were in good agreement with the experiment data. This validates that the cohesive zone is geometry-independent and can be used as the material parameter to apply in different geometry configurations. But these results should be used with caution as the same loading configuration was used (DCB). From the simulations, it was also shown that the CTOA constant value in the steady state is size-independent for the DCB specimens considered in this study. The CTOA value predicted from the 3D model was slightly higher than the value predicted from the 2D model.

A cohesive zone model was developed that allows for the prediction of mixed-mode crack growth resistance of adhesively bonded joints of varying joint thickness. It was demonstrated that crack path selection can be a major contribution to joint toughness if the mode mixity is high and if the bondline thickness is large. Then, the crack path develops freely. If however, the bondline thickness is small, the constraint imposed does not allow the crack path to develop, and the crack is forced into a mode I situation. Then, the toughness is that of a mode I-loaded joint. The increased toughness of the kinked crack paths enables the selection of different fracture modes, if a particular adhesive possesses such features. Then, a high crack path deflection will compete with alternative, lower toughness crack paths and a bimodal toughness response can be expected. The model presented is based on a basic energy criterion of crack advance and can be readily expanded to mode complex joint configurations. Experimental validation of the model is still necessary, despite that fact that the trends predicted by the model are in good agreement with general findings in related studies.

5. REFERENCES.

1. Guess, T.R., Reedy, E.D., Jr., and Slavin, A.M., "Testing Composite-to-Metal Tubular Lap Joints," *Journal of Composites Technology and Research*, Vol. 17, No. 2, 1995, pp. 117-124.

2. Guess, T.R., Reedy, E.D., Jr., and Stavig, M.E., "Mechanical Properties of Hysol EA-9394 Structural Adhesive," *SAND95-0229*, Sandia National Laboratories, Albuquerque, New Mexico, 1995.

3. Barenblatt, G.I., "The Mathematical Theory of Equilibrium Cracks in Brittle Fracture," *Advances in Applied Mechanics*, Academic Press, New York, Vol. 7, 1962, pp. 55-129.

4. Hillerborg, A., Modeer, M., and Petersson, P., "Analysis of Crack Formation and Crack Growth in Concrete by Means of Fracture Mechanics and Finite Elements," *Cement Concrete Research*, Vol. 6, 1976, pp. 773-782.

5. Needleman, A., "A Continuum Model for Void Nucleation by Inclusion Debonding," *Journal of Applied Mechanics*, Vol. 54, 1987, pp. 525-531.

6. Xu, X.P. and Needleman, A., "Numerical Simulations of Fast Crack Growth in Brittle Solids," *Journal of the Mechanic and Physics of Solids*, Vol. 42, 1994, pp. 1397-1434.

7. Remmers, J.J.C., de Borst, R., and Needleman, A., "The Simulation of Dynamic Crack Propagation Using the Cohesive Segments Method," *Journal of the Mechanics and Physics of Solids*, Vol. 56, 2008, pp. 70-92.

8. Song, J.H., Areias, P.M.A., and Belytschko, T., "A Method for Dynamic Crack and Shear Band Propagation With Phantom Nodes," *International Journal for Numerical Methods in Engineering*, Vol. 67, 2006, pp. 868-893.

9. Roy, S., Wang, Y., Park, S., and Liechti, K.M., "Cohesive Layer Modeling of Time-Dependent Debond Growth in Aggressive Environments," *Journal of Engineering Materials and Technology*, Vol. 128, 2006, pp. 11-17.

10. Hutchinson, J.W. and Evans, A.G., "Mechanics of Materials: Top-Down Approaches to Fracture," *Acta Materialia*, Vol. 48, 2000, pp. 125-135.

11. Tvergaard, V. and Hutchinson, J.W., "Toughness of an Interface Along a Thin Ductile Layer Joining Elastic Solids," *Philosophical Magazine A*, Vol. 70, 1994, pp. 641-656.

12. Tvergaard, V. and Hutchinson, J.W., "On the Toughness of Ductile Adhesive Joints," *Journal of the Mechanics and Physics of Solids*, Vol. 44, 1996, pp. 789-800.

13. Yang Q.D., Thouless, M.D., and Ward, S.M., "Numerical Simulations of Adhesive-Bonded Beams Failing With Extensive Plastic Deformation," *Journal of the Mechanics and Physics of Solids*, Vol. 47, 1999, pp. 1337-1353.

14. Yang Q.D., Thouless, M.D., and Ward, S.M., "Elastic-Plastic Mode-II Fracture of Adhesive Joints," *Journal of the Mechanics and Physics of Solids*, Vol. 47, 2001, pp. 1337-1353.

15. Xu, C., Siegmund, T., and Ramani, K., "Rate-Dependent Crack Growth in Adhesives II, Experiments and Analysis," *International Journal of Adhesion and Adhesives*, Vol. 23, No. 1, 2003, pp. 15-22.

16. Han, J. and Siegmund, T., "A Combined Experimental-Numerical Study on Crack Growth in a Carbon-Carbon Composite," *Fatigue and Fracture of Engineering Materials and Structures*, Vol. 6, 2006, pp. 632-645.

17. Kübler, J., "Fracture Toughness of Ceramics Using the SEVNB Method: Initial Results for Si3N4 of a Joint VAMAS/ESIS Round Robin," *9th International CIMTEC Conference*, Florence, Italy, June 14-19, 1998.

18. Rice, J.R., "A Path Independent Integral and the Approximate Analysis of Strain Concentration by Notches and Cracks," *Journal of Applied Mechanics*, Vol. 35, 1968, pp. 379-386.

19. Sørensen, B.F. and Jacobsen, T.K., "Determination of Cohesive Laws by the *J* Integral Approach," *Enginerring Fracture Mechanics*, Vol. 70, 2003, pp. 1841-1858.

20. Tamuzs, V., Tarasovs, S., and Vilks, U., "Delamination Properties of Translaminar-Reinforced Composites," *Composites Science and Technology*, Vol. 63, 2003, pp. 1423-1431.

21. Lin, G., Kim, Y.J., Cornec, A., and Schwalbe, K.H., "Fracture Toughness of a Constrained Metal Layer," *Computational Materials Science*, Vol. 9, No. 1-2, 1997, pp. 36-47.

22. Tvergaard, V. and Hutchinson, J.W., "The Relation Between Crack Growth Resistance and Fracture Process Parameters in Elastic-Plastic Solids," *Journal of the Mechanics and Physics of Solids*, Vol. 40, 1992, pp. 1377-1397.

23. Tvergaard, V. and Hutchinson, J.W., "The Influence of Plasticity on Mixed Mode Interface Toughness," *Journal of the Mechanics and Physics of Solids*, Vol. 41, 1993, pp. 1119-1135.

24. Ma, L., Lam, P.W., Kokaly, M.T., and Kobayashi, A.S., "CTOA of a Stable Crack in a Thin Aluminum Fracture Specimen," *Engineering Fracture Mechanics*, Vol. 70, 2003, pp. 427-442.

25. Khoo, T.T., "Effect of Bondline Thickness of Mixed Mode Fracture of Adhesive Joints," Purdue University, M.S. Thesis, December 2006.